Measurement and Simulation of Mechanical and Optical Properties of Sputtered Amorphous SiC Coatings

G. Favaro,[1] M. Bazzan,[1,*] A. Amato,[2] F. Arciprete,[3,4] E. Cesarini,[4] A.J. Corso,[5]
F. De Matteis,[3,4] T.H. Dao,[3,4] M. Granata,[6] C. Honrado-Benítez,[7] N. Gutiérrez-Luna,[7]
J.I. Larruquert,[7] G. Lorenzin,[1] D. Lumaca,[3,4] G. Maggioni,[1] M. Magnozzi,[8] M.G. Pelizzo,[1]
E. Placidi,[9] P. Prosposito,[3,4] and F. Puosi[10]

[1]*Università di Padova, Padova I-35131, Italy*

[2]*Université de Lyon, Université Claude Bernard Lyon 1, CNRS, Institut Lumière Matière, Villeurbanne F-69622, France*

[3]*Università di Roma Tor Vergata, Roma I-00133, Italy*

[4]*INFN, Sezione di Roma Tor Vergata, Roma I-00133, Italy*

[5]*CNR, Istituto di Fotonica e Nanotecnologie, Padova I-35131, Italy*

[6]*Laboratoire des Matériaux Avancés - IP2I, CNRS, Université de Lyon, Université Claude Bernard Lyon 1, Villeurbanne F-69622, France*

[7]*GOLD-IO-CSIC, Serrano 144, Madrid S-28006, Spain*

[8]*Università di Genova, Genova I-16146, Italy*

[9]*Università di Roma "La Sapienza", Roma I-00185, Italy*

[10]*INFN, Sezione di Pisa, Pisa I-56127, Italy*

In this work we report on the extensive characterization of amorphous silicon carbide (*a*-SiC) coatings prepared by physical deposition methods. Our investigation is performed within the perspective application of *a*-SiC as an optical material for high-precision optical experiments and, in particular, in gravitational wave interferometry. We compare the results obtained with two different sputtering systems [a standard radio frequency (rf) magnetron sputtering and an ion-beam sputtering] to grasp the impact of two different setups on the repeatability of the results. After a thorough characterization of structural, morphological, and compositional characteristics of the prepared samples, we focus on a detailed study of the optical and mechanical losses in those materials. Mechanical losses are further investigated from a microscopic point of view by comparing our experimental results with molecular dynamic simulations of the amorphous SiC structure: first we define a protocol to generate a numerical model of the amorphous film, capturing the main features of the real system; then we simulate its dynamical behavior upon deformation in order to obtain its mechanical response.

I. INTRODUCTION

Crystalline silicon carbide (SiC) is one of the most mature among the wide band-gap semiconductors (2.0 eV $\lesssim E_g \lesssim$ 7.0 eV where E_g is the energy gap) for high-temperature, high-power, high-frequency, and radiation-hardened applications, due to its favorable physical properties and its commercial availability [1–5]. One of the most distinctive features of SiC is the rich variety of its crystal forms. SiC is part of a family of materials which exhibit a one-dimensional polymorphism, called polytypism. An almost infinite number of SiC polytypes are possible, and approximately 200 polytype, differentiated by the stacking sequence of each tetrahedrally bonded Si—C bilayer, have already been discovered [6]. Even though individual bond lengths are nearly identical, the crystal symmetry is determined by the stacking periodicity. This variety of structural arrangements is mirrored by the large variability of SiC physical properties such as optical band gap, thermal and electrical conductivity, and so on.

More recently, silicon carbide has attracted a renewed interest in its amorphous form (*a*-SiC) as a material for optical and optoelectronic applications, as well as for more cutting-edge research [7,8]. In the case of the amorphous structure, the variety of the allowable bond configurations offered by the SiC polytypism together with the possibility

---

*Author to whom correspondence should be addressed. marco.bazzan@unipd.it

of doping control allow the optical and mechanical properties to be tuned in situations where high refractive index, mechanical stability, and low absorption is required.

In particular, *a*-SiC could have the potential to address very critical issues in high-precision optical experiments such as interferometric gravitational-wave detectors (GWDs) [9], optomechanical resonators [10], and frequency standards [11]. Those experiments, and, in particular, GWDs such as advanced LIGO [12], advanced Virgo [13], and KAGRA [14], require high-reflection (HR) optical coatings made up of Bragg reflectors of alternating layers of low- and high-refractive-index materials. Despite the superb optical properties of the coatings used in present GWDs [15–18], HR coatings still constitute a severe limitation for further sensitivity improvement in GWDs due to their thermal noise issue. The presence of thermally driven random structural relaxations distributing the thermal energy of the normal modes of vibration across a wide frequency range, gives rise to Brownian *coating thermal noise* (CTN) [19–21]. The power spectral density of such thermally induced surface fluctuations is determined by the rate of energy dissipation in the coating material, which is measured by the mechanical loss angle φ, as stated by the fluctuation-dissipation theorem [22]. Currently high-index materials contribute around one order of magnitude more than low-index materials to CTN. In the last two decades, a considerable research effort has been committed to finding an alternative high-index material featuring both low mechanical and optical losses, see Refs. [23,24] and references therein.

In this paper we report on the optical and mechanical properties of sputtered amorphous silicon carbide (*a*-SiC) thin films, and we discuss their potential application in current and future GWDs. The main goal of our research is to determine precisely the properties of *a*-SiC from the standpoint of GWDs' requirement, taking into account that the deposition method may strongly affect the structure and thus the properties of the optical film. In order to elucidate how strongly the obtained films are influenced by the deposition methods, we compare coatings produced in two different sputtering systems: (i) a home-made standard laboratory magnetron sputtering apparatus and (ii) an ion-beam sputtering system, which is the technology of choice to produce the tantalum pentoxide-titanium dioxide mixture (Ta_2O_5-TiO_2, also known as *titania-doped tantala*, high index) and silicon dioxide (SiO_2, *silica*, low index) thin coating layers presently used in the mirrors of GWDs [15,25]. We determine the physicochemical characteristics of the *a*-SiC thin-film samples by a wide range of techniques, with particular attention to their complex refractive index, surface quality, and mechanical loss angle in order to assess the potential of SiC as a material for GWDs. Finally, in order to obtain a microscopic insight on the material, the experimental results have been compared with the results of an atomistic calculation

simulating the amorphous structure of SiC and its mechanical properties.

II. SAMPLE PRODUCTION

Thin layers of amorphous SiC have been deposited on different substrates for different purposes: (i) silicon wafers ($\varnothing$ 25.4 mm, 5 mm thick) and sapphire substrates ($\varnothing$ 25.4 mm, 5 mm thick) as witness samples to measure the optical properties, stoichiometry and structure of the coatings, (ii) amorphous carbon (*a*-C) with a thin layer of MS gold (Au) to perform accurate Rutherford back-scattering spectrometry experiments, (iii) fused-silica disks ($\varnothing$ 50 mm, 0.35 to 1 mm thick) to measure the coating mechanical properties.

Due to the nature of the mechanical loss measurements, which are particularly sensitive to the experimental conditions, the fused-silica disks are prepared according to the following specific protocol: (i) in order to release the internal stress due to manufacturing and induce relaxation, the bare disks are annealed in air at 900 °C for 10 h; (ii) their intrinsic mechanical loss is measured, prior to coating deposition; (iii) in order to cancel out the coating-induced curvature that would affect the measurement of their resonant frequencies, thin films of equal thickness are grown on both their optically polished surfaces.

After deposition, in some selected cases, the coated samples are annealed to relax internal stresses and improve the coating optical properties. The effects of this treatment from the standpoint of the optical properties are discussed below.

In order to estimate how much the properties of the deposited materials are dependent upon the specific growth conditions, we compare the results obtained using two different sputtering systems. The first one is a standard radio-frequency magnetron-sputtering (MS) setup located inside Laboratori Nazionali di Legnaro [26] (INFN-LNL). The second is an ion-beam sputtering system (IBS) located at the GOLD facility of the Instituto de Óptica Daza de Valdés [27] (IO-CSIC).

A. Magnetron-sputtering samples

In our MS system, a commercial 2-in. SiC target with a purity of 99.999% is used within a radio-frequency source (Torus 2C Kurt J. Lesker) operated at 100 W by means of an appropriate radio-frequency power supply (RFX600 Advanced Energy). All the processes are performed in an Ar atmosphere: the ionized Ar atoms bombard the SiC target with an energy sufficient to produce the sputtering of the source elements, favoring the deposition of an amorphous film of SiC on the substrate to be coated. The value of the pressure inside the chamber is around 8×10^{-7} mbar before the injection of argon and around 6×10^{-3} mbar during the sputtering process. The distance between the target and the substrate is of 14 cm and the flux of argon in the chamber is 17 sccm for all depositions. The substrates

are mounted on a rotating sample holder for improved coating thickness homogeneity. The velocity of rotation is set at 30 rpm for all the depositions. The thickness of the coatings deposited in this system ranges from 40 to 400 nm, with a deposition rate of 0.017 nm/s. In order to modify the film stoichiometry, a varying number of Si pieces are placed on the SiC target for some deposition runs. This allowed us to produce a set of samples with different Si:C ratios, in order to explore the influence of the composition on the optical properties.

B. Ion-beam-sputtering samples

Prior to deposition, the residual pressure inside the coater vacuum chamber is less than 3×10^{-8} mbar. Ar is used as the sputtering gas, the total pressure is 1×10^{-3} mbar during the coating process. Sputtering ions are produced by means of a 3-cm diameter hollow cathode ion gun working with a hollow cathode neutralizer, both without filament in order to minimize contamination. Energy and discharge beam current of the ions are 1.0 keV and 50 mA, respectively, yielding a deposition rate of 0.05 nm/s, as measured with a quartz crystal monitor. A 96.5-mm diameter SiC target of 99.9995% purity is used, mounted in a multitarget rotating holder cooled down with water. Substrates during rotation are kept at a distance of 21 cm above the target, with the ion beam impinging on the latter at 45°. Each thin film is grown separately, but all coating samples are grown under identical conditions.

III. PHYSICOCHEMICAL CHARACTERIZATIONS

From a structural point of view, as-deposited films are in a nonequilibrium state. During the deposition they can eventually heat up so that some structural evolution may take place bringing to the formation of nanosized crystalline regions. It is necessary to check that the deposited films are still in a fully amorphous state because the formation of nanocrystals is generally detrimental from the point of view of optical and mechanical properties. Grazing-incidence x-ray diffraction (GIXRD) is a well-known technique able to detect the formation of crystalline regions inside a thin film. On the other hand, x-ray reflectivity (XRR) analyses offer access to complementary informations, such as the thickness and the density of the amorphous film. Both these techniques are performed using a Philips MRD diffractometer equipped with a Cu tube operated at 40 kV and 40 mA. The beam is collimated and partially monochromatized by a parabolic multilayer mirror, while the detector is equipped with a parallel plate collimator (PPC) to define the angular acceptance. To perform XRR measurements an additional high-resolution four-bounce symmetric Bartels monochromator is mounted on the primary optics and the PPC is replaced with a three-bounce symmetric analyzer. Both

those devices exploit Bragg diffraction from the (2 2 0) crystallographic planes of a set of nearly perfect Ge single crystals to produce a highly monochromatic ($\Delta\lambda/\lambda = 10^{-5}$) and narrowly collimated ($\Delta\theta = 0.0039$ deg) x-ray beam.

The surface morphology of the deposited films is studied by a Veeco Multiprobe Nanoscope IIIa atomic force microscope (AFM). Topographies are acquired in tapping mode (amplitude modulation) by means of a silicon tip with a stiffness of 42 N/m (resonance frequency around 300 kHz) and radius of curvature below 7 nm. The measurements are performed in the MBE laboratory in the Physics Department of University of Rome Tor Vergata.

The composition of the films is investigated by Rutherford back-scattering spectrometry (RBS) using a 2.0 MeV 4He+ beam at the Van der Graaf accelerator at the INFN-LNL with a 160° scattering angle, normal incidence, and a silicon solid-state detector.

A. Results

1. X-ray analysis

In Fig. 1 the results of the GIXRD and XRR analyses are presented on two representative samples prepared by the MS and IBS deposition systems on two different substrates. The GIXRD spectra are recorded for different values of the incidence angle $\omega = 1, 2, 3°$ in order to compare a different penetration depth of the x-ray beam. In all cases, the samples did not demonstrate any diffraction peak confirming that the grown SiC layers are amorphous. Note that the difference between the two spectra reported in Figs. 1(a) and 1(b) is due to the different substrates: the former is obtained from a film deposited on amorphous silica, which contributes to the diffracted signal with the smooth diffraction pattern typical of this material; the second sample has a crystalline sapphire substrate, which does not induce any significant background.

The XRR analysis allows determination of the average density and the surface roughness for the two films. For films thinner than 500 nm, our reciprocal space resolution also allows us to measure thickness fringes and hence determine the film thickness from an analysis of the curve. Experimental data of the MS sample, shown in Fig. 1(c), is well fit with a simple single-layer model using the REFLEX software [28]. The obtained average density, $\rho = (2.82 \pm 0.05)$ g/cm^3, is in agreement with previous works [29], and the roughness resulted in $\sigma = (2.3 \pm 0.1)$ nm. In the case of the IBS sample, the model is slightly more complex as it required the introduction of a thin low-density cap layer of about 13 nm to model the low-frequency modulations visible in Fig. 1(d). The results for that layer are $\rho = (2.87 \pm 0.01)$ g/cm^3 and $\sigma = (0.5 \pm 0.1)$ nm, so the MS and IBS samples have a very similar density but the IBS sample has a much smoother surface. Note however that, besides being deposited on different
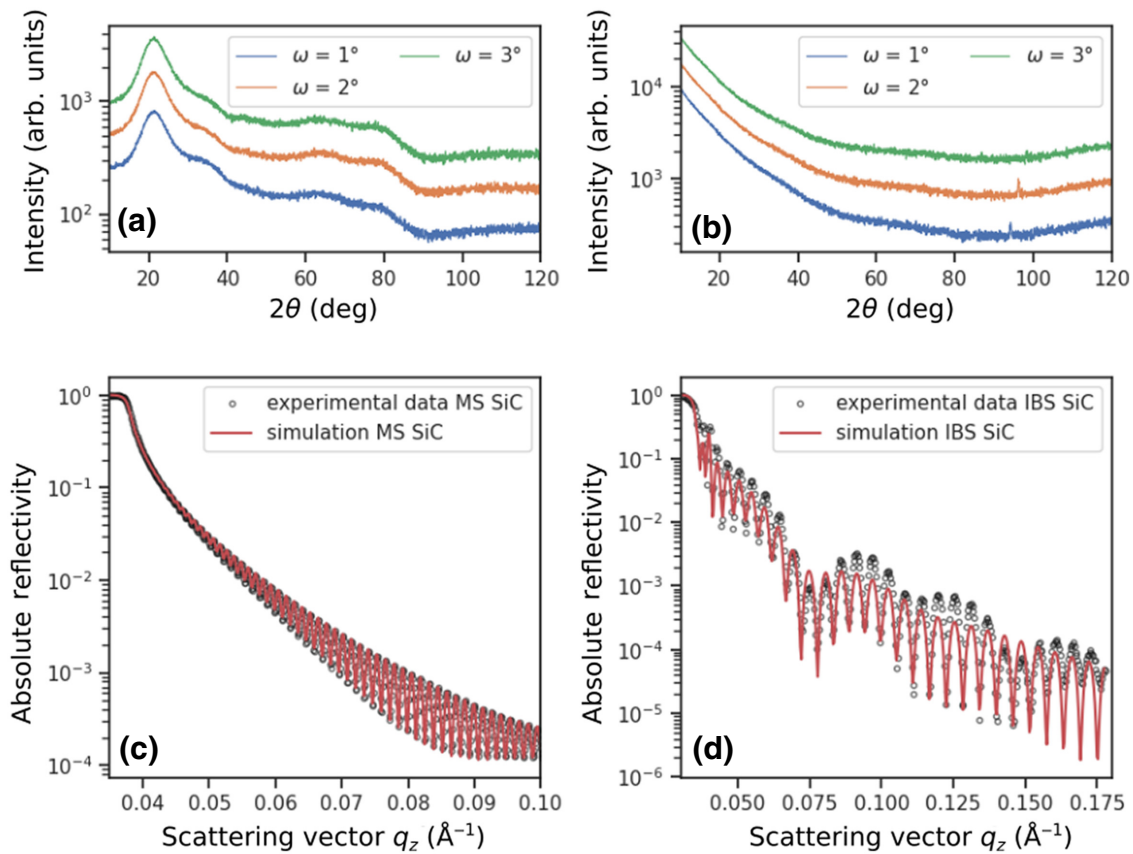
FIG. 1.   GIXRD and XRR spectra for two *a*-SiC thin-film samples prepared by MS and IBS on different substrates. (a) GIXRD of MS *a*-SiC on a SiO$_2$ substrate; (b) GIXRD of IBS *a*-SiC on a Al$_2$O$_3$ substrate; (c) XRR of the same sample as in (a); XRR of the same sample as in (b). The red lines in (c),(d) are model fits.

substrates, those values are obtained in two samples with significantly different thicknesses, $t = (423.1 \pm 0.1)$ nm for the MS sample and $t = (104.3 \pm 0.1)$ nm for the IBS sample, as measured by XRR curves. Those aspects may also contribute to the observed difference in the surface roughness [30].

2. Atomic force microscopy

MS samples are also characterized by AFM, in order to investigate the details of the surface topography. The results presented in Fig. 2 show that MS samples exhibit a surface morphology characterized by raw textures, probably related to the substrate polishing. In excellent agreement with XRR analysis, the RMS roughness measured by AFM is around 2.2 nm for all the examined maps. On the very surface, small grains with average height and diameter, respectively, of 5 and 20 nm can be observed [as pointed out in panel (b) of Fig. 2].

3. Rutherford backscattering spectrometry

Figure 3 compares experimental RBS spectra of two *a*-SiC samples, grown by MS and by IBS on different substrates.

The 50-nm-thick MS sample is deposited on a special gold-coated amorphous carbon substrate, especially designed for RBS measurements; the additional 80-nm-thick Au layer allows us to separate in energy the signal of the *a*-SiC film from that of the substrate in order to simplify the analysis. In Fig. 3(a), the first part of the spectrum between 200 and 400 keV results from collisions of incident α particles reaching the carbon substrate after losing some energy by passing through the first layers of the sample. The peaks due to collisions with the C and Si atoms in the film are clearly visible (the peak related to collisions with Au atoms is outside the range displayed in
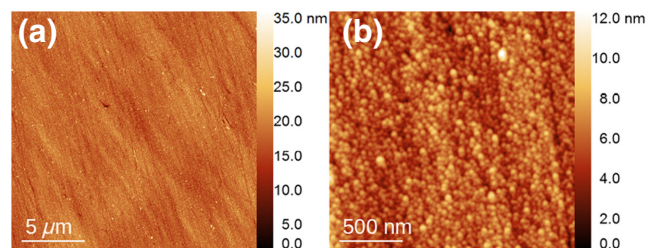

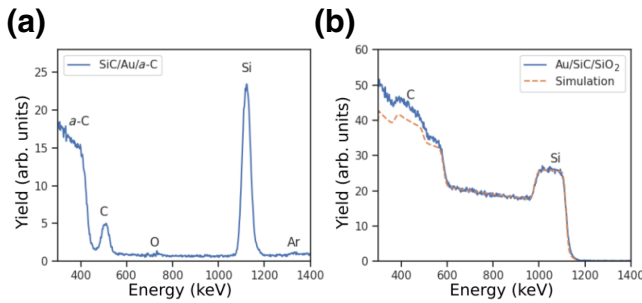FIG. 2.   AFM topographies of the SiC surface.

FIG. 3. (a) RBS spectrum for the MS sample deposited on a Au/C substrate; (b) RBS spectrum for an IBS sample deposited on a SiO$_2$ substrate.

the figure). The areal density and the composition of the deposited films is thus obtained by integration of the peak area. The average areal density of the measured MS samples is $(2.8 \pm 0.1) \times 10^{17}$ SiC molecules per cm^2 which, taking into account the film thickness, results in a density of $\rho = (2.9 \pm 0.1)$ g/cm^3, in agreement with the results obtained from the XRR data. Some contamination of other elements has also been detected as traces, mainly O (around 2 mol.%) while other contamination (Ar from the sputtering atmosphere and Fe from the target holder) are below 1 mol.%. The Si:C ratio of an as-deposited MS sample is 0.74 ± 0.03 (while a stoichiometric sample would be expected to have Si:C = 1), showing a tendency towards Si deficiency with respect to the stoichiometric composition. By adding some pieces of Si cut from a commercial Si wafer on the target, the Si:C ratio of the deposited films could be varied between 0.74 ± 0.03 and 1.15 ± 0.03, providing a set of samples with different stoichiometries to be used in the next analysis.

In the case of IBS samples, we did not have the possibility to coat the special substrates with the film to be analyzed and we had to use some "regular" samples, deposited on standard substrates. In this case, the RBS spectrum cannot be analyzed by integration of the element peaks as the signals from the different elements of the film overlap with the substrate signal. Moreover, for a nonconducting substrate like SiO$_2$, to avoid the sample charging and producing artifacts in the RBS spectrum, it is necessary to deposit a conducting layer on top of the samples to be analyzed. For this reason, we deposit an additional Au layer on top of the SiC coating. An example of RBS data obtained with this configuration can be seen in Fig. 3(b), which presents the spectrum of an IBS sample grown on a SiO$_2$ substrate. In this case, the analysis can be performed by fitting the experimental spectrum with numerical simulations obtained by the RUMP software [31], at the price of a higher uncertainty in the elemental analysis. In Fig. 3(b) the signal of Si and C coming from the film is clearly visible, while the incorporation of other elements such as oxygen is not visible. The areal density of the

IBS film given by the analysis is $(9.3 \pm 0.1) \times 10^{17}$ SiC molecules per cm^2. By dividing by the film thickness, one gets a film density of $\rho = (2.8 \pm 0.2)$ g/cm^3, once again in agreement with XRR data. Differently from what is observed with MS samples, as-deposited IBS samples appear to be more stoichiometric, with a Si:C ratio close to 1.

IV. OPTICAL PROPERTIES

Optical spectroscopic ellipsometry (SE) is an established technique for the study of the optical properties of thin films and, in particular, of gravitational-wave detector coatings [15,17,32]. The optical characterization of *a*-SiC coating samples is performed using a J. A. Woollam Co. Variable Angle Spectroscopic Ellipsometer (VASE), which exploits the rotating analyzer configuration. The setup is equipped with a computer-controlled compensator (AutoRetarderTM), which allows measurement of the two experimental parameters Ψ and Δ. These values are related to the ratio of Fresnel reflection coefficients for *p*- and *s*-polarized light. Such a ratio can be expressed as a complex number, with $tan(\Psi)$ and Δ being its modulus and argument, respectively.

Ψ and Δ are functions of the complex refractive index and of the sample thickness, in the whole range 0–360° without ambiguity. Spectroscopy ellipsometry measurements are performed between 300–1700 nm at incidence angles of 55°, 60°, and 65° in the probed spectral range in order to maximize the sensitivity around Brewster's angle. Furthermore, the same setup adjusted in transmission mode allows for a direct absorbance measurement on the same spectral range. Since the absorbance is closely related to the absorption coefficient defined as $\alpha = 4\pi/(\lambda)\kappa$ (where κ is the imaginary part of the refractive index), the absorption and SE measurements can be combined in a global minimization analysis using the J. A. Woollam Co. WVASE software package. A Tauc-Lorentz dielectric function ($\varepsilon_2^{(\mathrm{TL})}$) with an additional Lorentzian component ($\varepsilon_2^{(L)}$) [33] is used to model the imaginary part of the dielectric constant (ε_2) of all the samples in the investigated spectral range:

$$\varepsilon_2(E) = \varepsilon_2^{(\mathrm{TL})}(E) + \varepsilon_2^{(L)}(E),$$

$$\varepsilon_2^{(\mathrm{TL})}(E) = A^{(\mathrm{TL})} \frac{(E - E_g)^2}{E^2}$$

$$\times \frac{B_r E_n^2 E}{(E^2 - E_n^2)^2 + (B_r E)^2} \Theta(E - E_g),$$

$$\varepsilon_2^{(L)}(E) = A^{(L)} \frac{C E_0 E}{(E^2 - E_0^2)^2 + (CE)^2}. \quad (1)$$

The Lorentzian component $\varepsilon_2^{(L)}(E)$ is characterized by the peak energy E_0 and the width C; for the Tauc-Lorentz
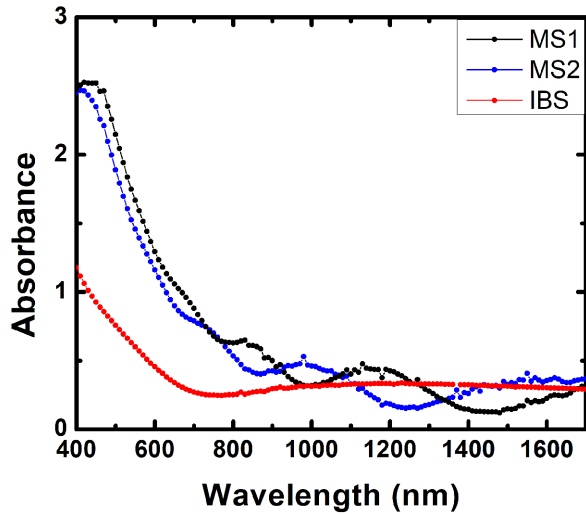
FIG. 4.   Absorption spectra of two *a*-SiC samples grown via MS on a 0.1-mm-thick silica substrate and of an *a*-SiC sample grown via IBS on a 5-mm-thick sapphire substrate. All films have a Si:C ratio compatible with 1 within experimental uncertainty.
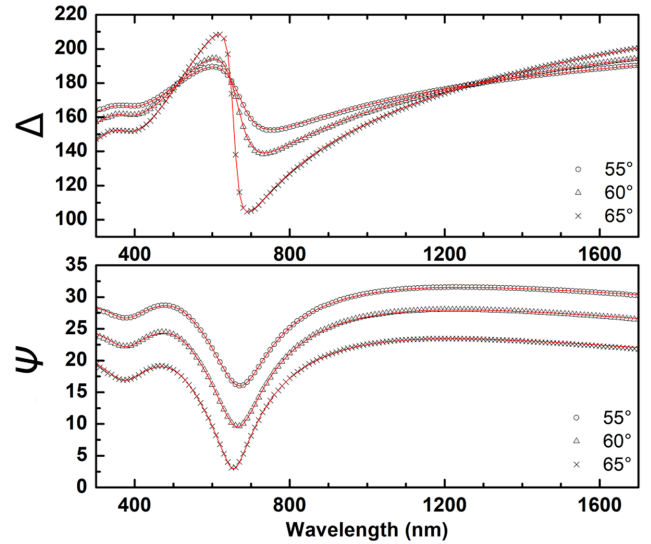

FIG. 5.   Spectroscopic ellipsometry of an *a*-SiC sample grown by means of IBS on a 5-mm-thick sapphire substrate. The experimental data are measured at an incidence angle of 55° (circles), 60° (triangles), and 65° (crosses). The red lines are fit curves obtained by the global optimization of the dielectric model function.

function $\varepsilon_2^{(TL)}$, E_g is the gap energy, E_n the peak energy, and B_r the width of the dielectric function, while $\Theta(E)$ is Heaviside's step function. The real part of the dielectric constant $[\varepsilon_1(E)]$ is then obtained by Kramers-Kronig transformation of $\varepsilon_2(E)$. The surface roughness is modeled within the effective medium approximation (EMA) as a 50:50 mix of SiC and voids; this layer includes also the effect of surface oxide [34].

A. Results

Figure 4 shows the absorption spectra of two MS samples deposited on a 0.1-mm-thick silica substrate and of an IBS sample deposited on a 5-mm-thick sapphire substrate. For this comparison, we choose all the samples to have a Si:C ratio equal to 1 within experimental uncertainty. The nominal thicknesses of the *a*-SiC layers are, respectively, 500, 400, and 100 nm. A typical comparison between the experimental SE data and the fitted model function is shown in Fig. 5 for the IBS sample grown on a sapphire substrate. The parameters of the dielectric model [Eq. (1)] are reported in Table I for all samples.

Optical data indicate that the optical gap E_g ranges from 1.8 to 2.25 eV, and confirms the higher roughness of MS samples compared to IBS ones, in agreement with XRR measurements. This larger roughness explains the higher absorbance visible in Fig. 4 for MS samples.

Exemplary plots of the refractive index and absorption coefficient as a function of the wavelength measured in two different positions and on two different MS samples are reported in Fig. 6. Although a certain variability is present from point to point and on the two different samples, the values of the n and κ optical constants at 1064 nm are

around 3.0 and 0.1, respectively. Those results fall within the quite wide range of optical-constant data reported in the literature for SiC, corresponding to different deposition techniques and conditions [35–37]. Yet this result indicates that our as-deposited SiC samples are characterized by a very high absorption level, several orders of magnitude higher than typical values encountered in other optical coatings for such as, e.g., tantala [16,18].

Other MS samples with different compositions of Si:C ranging from 0.74 to 1 are analyzed as well (data not shown). The optical properties of the different as-deposited samples exhibit a certain degree of variability up to 10%,

TABLE I.   Fitting parameters for the Tauc-Lorentz (TL) plus Lorentzian (L) dielectric model for the *a*-SiC samples grown via MS and IBS. MSE is the mean square error between the fitted model and experimental Δ and Ψ.

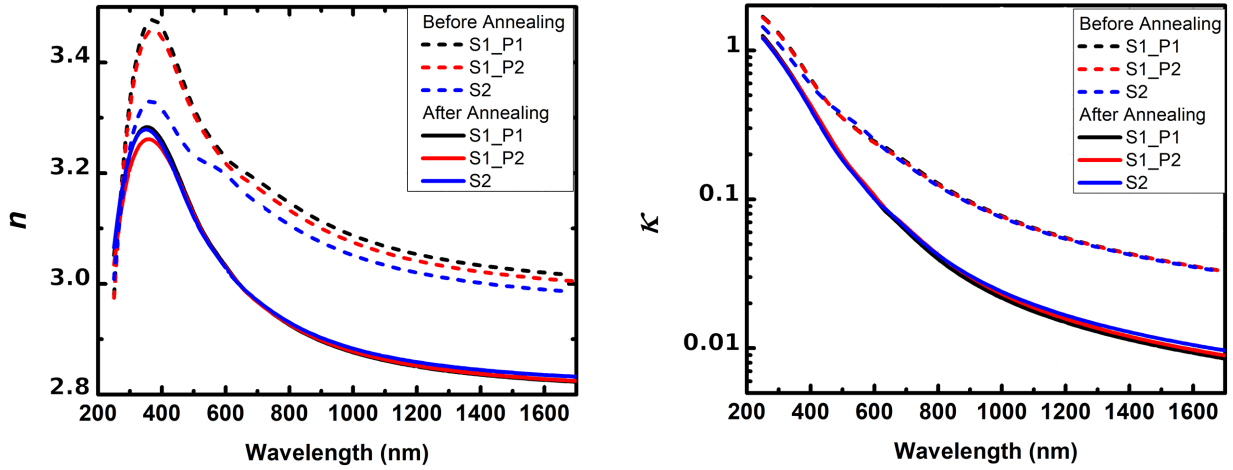|	Sample	MS 1	MS 2	IBS
	Substrate	SiO_2 0.1 mm	SiO_2 0.1 mm	Al_2O_3 5 mm
	MSE	7.7	8.3	1.4
	Roughness (nm)	8.3 ± 0.2	5.8 ± 0.2	1.50 ± 0.03
	Thickness (nm)	401.8 ± 0.7	478.8 ± 0.8	101.48 ± 0.03
TL	$A^{(TL)}$	150 ± 9	208 ± 10	244 ± 5
	E_n (eV)	5.7 ± 0.2	5.3 ± 0.1	4.80 ± 0.04
	E_g (eV)	1.79 ± 0.04	2.01 ± 0.03	2.25 ± 0.01
	B_r (eV)	7 ± 1	9.1 ± 1.0	6.8 ± 0.2
L	$A^{(L)}$	1.42 ± 0.09	1.73 ± 0.07	2.74 ± 0.04
	E_0 (eV)	2.26 ± 0.05	2.33 ± 0.03	2.66 ± 0.01
	C (eV)	1.40 ± 0.03	1.29 ± 0.03	1.44 ± 0.01

FIG. 6.   Real (left) and imaginary (right) parts of the refractive index of two MS a-SiC samples. Sample S1, which is measured at two different positions P1 (black) and P2 (red), and sample S2 (blue) are annealed for 10 h at 500 °C with heating and cooling rates of 100 °C/h: the optical constants are reported before (dashed) and after (full) annealing.

but the observed variations do not show any clear correlation with the sample composition.

After 6 months, the two MS samples are annealed at 500 °C in air for 10 h with a ramp rate of 1.6 °C/min. The temperature is chosen in order to allow relaxation of the amorphous phase, avoiding any microcrystallization process [38]. Figure 6 shows the effect of the annealing on the optical constants for MS sample 1 (measured at two points) and MS sample 2. Both the real and imaginary parts of the refractive index decrease to about 2.9 and 0.02, respectively, at 1064 nm and become much less scattered, hinting that the different optical behaviors observed in the as-deposited samples are related to an initial unrelaxed state bearing a certain level of spatial inhomogeneity. Still, in spite of a considerable decrease of the imaginary part of the refractive index κ upon annealing, the absorption remains way above the level of 10^{-8}–10^{-7} required for GW detectors.

V. MECHANICAL PROPERTIES

Three fused-silica disks with a nominal diameter of 50 mm are used for the characterization of the coating mechanical properties: disks A and B, 1 mm thick, coated with IBS a-SiC thin films, are measured at the Laboratoire des Matériaux Avancés (LMA); disk C, 0.35 mm thick, coated with MS a-SiC thin films, is measured at Università degli Studi di Roma Tor Vergata (UniToV). All the samples had nearly stoichiometric composition, as verified via RBS measurements (see Sec. III A 3). XRR data is used to estimate the density and thickness of the thin films (see Sec. III A 1).

We use the ring-down method [39] to measure the frequency f and ring-down time τ of the first vibrational modes of each disk, before and after the coating deposition,

and calculated the coating loss angle

$$\varphi_c = \frac{\varphi + (D-1)\varphi_0}{D}, \tag{2}$$

where $\varphi_0 = (\pi f_0 \tau_0)^{-1}$ is the measured loss angle of the bare substrate, $\varphi = (\pi f \tau)^{-1}$ is the measured loss angle of the coated disk. D is the measured frequency-dependent *dilution factor* [40],

$$D = 1 - \frac{m_0}{m}\left(\frac{f_0}{f}\right)^2, \tag{3}$$

where (m_0, m) is the disk mass before and after coating deposition, respectively. We measure modes from approximately 2.5 kHz to approximately 38.5 kHz for disks A and B and from approximately 900 Hz to approximately 18 kHz for disk C, in a frequency band, which partially overlaps with the detection band of ground-based gravitational-wave detectors (10–10^4 Hz). In order to avoid systematic damping from suspension and ambient pressure, we use two clamp-free, in-vacuum gentle nodal suspension (GeNS) systems [41], shown in Fig. 7. This kind of system is currently the reference solution of the Virgo and LIGO Collaborations for performing loss angle measurements on thin films [15,42].

The diameter of all disks is measured with a caliper. Mass values m_0 and m of disks A and B are measured with an analytical balance, before and after coating deposition. For disk C, only the mass value m after coating could be measured with an analytical balance; its mass before coating is then calculated as $m_0 = m - m_c$, where the coating mass m_c is estimated from known coating properties: thicknesses measured via spectroscopic ellipsometry (see Sec. IV A), top and bottom surface areas estimated from
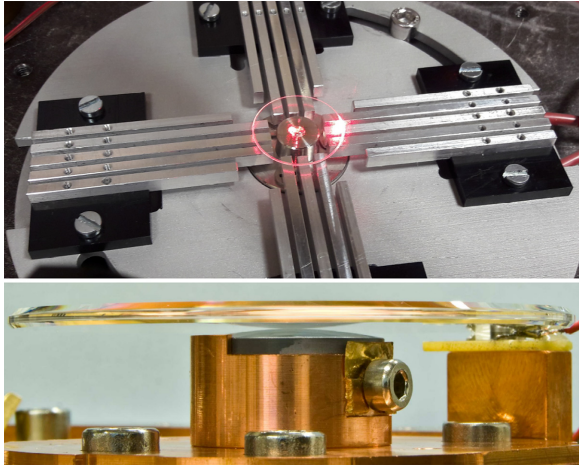
FIG. 7. GeNS systems used at Università degli Studi di Roma Tor Vergata (top) and at Laboratoire des Matériaux Avancés (bottom) to measure the mechanical properties of thin films.

diameter measurements, and density measured via XRR analysis (see Sec. III A 1).

By definition, the measure dilution factor D of Eq. (3) is very sensitive to variations of frequencies and masses [43], so we take special care to prevent the curvature of the disks induced by the presence of the coating layers by performing a double deposition on both the substrate faces, as explained in Sec. II, and monitor the temperature of the disks during the ring-down measurements. Indeed, the frequency ratio in Eq. (3) depends on the sample Young modulus, which is in turn temperature dependent. To keep track of this issue, each GeNS setup has its temperature probe: right under the copper base plate of the LMA system (visible in the foreground of Fig. 7), and fixed to the optical bench at UniToV. The GeNS system at LMA is installed in a clean room where the temperature is stabilized to $(21.9 \pm 0.5)\,°C$, whereas the temperature of the GeNS system at UniToV is not stabilized. Therefore, in order to obtain resonant frequency values $f(T_0)$ at a reference temperature T_0, $f(T)$ values measured at UniToV are corrected according to the following equation:

$$f(T_0) = \frac{f(T)}{1 + \eta T + q},\tag{4}$$

where $\eta \sim 9.5 \times 10^{-5}\,K^{-1}$ and $q \sim 1.9 \times 10^{-3}$ are coefficients we previously measured on nominally identical fused-silica disks. Loss angle measurements are usually significantly faster (10 to 60 min) for coated samples, compared to those of bare substrates (up to several hours), because of the higher loss angle; thus, during the measurement of disk C after coating, we assume that the temperature of the GeNS system at UniToV could be considered fairly constant and equal to $T_0 = 24.02 \pm 0.08\,°C$. We then correct the mode-frequency values of the bare

TABLE II. Disks used to characterize the mechanical properties of the a-SiC sputtered thin films: diameter $\varnothing$, thickness d_0, mass m_0 before coating, mass m after coating, coating thickness d_i on each side ($i = 1, 2$). Mass value m_0 for disk C is an estimation derived from known properties (see text for more details). Disks A and B are coated with IBS thin films, disk C with MS thin films.

	A	B	C
m_0 (g)	4.6453 ± 0.0003	4.6448 ± 0.0003	1.561 ± 0.001
m (g)	4.6472 ± 0.0002	4.6468 ± 0.0002	1.566 ± 0.001
$\varnothing$ (mm)	49.93 ± 0.01	49.92 ± 0.01	50.8 ± 0.1
d_0 (mm)	1.08 ± 0.01	1.08 ± 0.01	0.34 ± 0.04
d_1 (nm)	220 ± 5	221 ± 5	430.7 ± 0.3
d_2 (nm)	220 ± 5	222 ± 5	422.5 ± 0.3

disk C using Eq. (4), thus slightly changing them as if they had been measured at the same temperature T_0 of the measurements performed after coating. We finally use that set of corrected values in Eqs. (3) and (2) to estimate the coating loss angle of the MS a-SiC thin films grown on disk C. This correction is critical, whenever mode frequencies are measured in a system where temperature may drift [43]. Further details about our GeNS systems are available elsewhere [41,44].

A. Results

The main features of the disks used for the measurements of the coating mechanical properties are presented in Table II. Figure 8 shows the measured loss angles as a function of frequency: the loss angle of the IBS a-SiC coatings decreases from about 10^{-3} to 8×10^{-4} rad, whereas the loss angle of the MS a-SiC coatings increases from about 6×10^{-4} to 10×10^{-4} rad. Such different behavior might be explained by the nature of the coating samples, due to the different growth techniques. For instance, AFM measurements (see Fig. 2) show that MS samples present a grainy structure, which is not observed in IBS ones, indicating a difference in the film microstructure, which could possibly reflect the difference in their mechanical behavior.

For the MS a-SiC sample, we could fit a power-law model [45–47]

$$\varphi_c(f) = a \left(\frac{f}{10\,\text{kHz}} \right)^b \tag{5}$$

to our data via least-squares linear regression. This is not possible for the data of the IBS samples, whose frequency dependence cannot be explained on the basis of currently well-known structural relaxation models. Table III lists the obtained best-fit parameters (a, b), together with the best-fit estimations of coating Young modulus Y and Poisson ratio ν of the IBS a-SiC coatings, obtained by fitting finite-element simulations to the measured dilution factor via least-squares numerical regression [15,44]. For disk C,
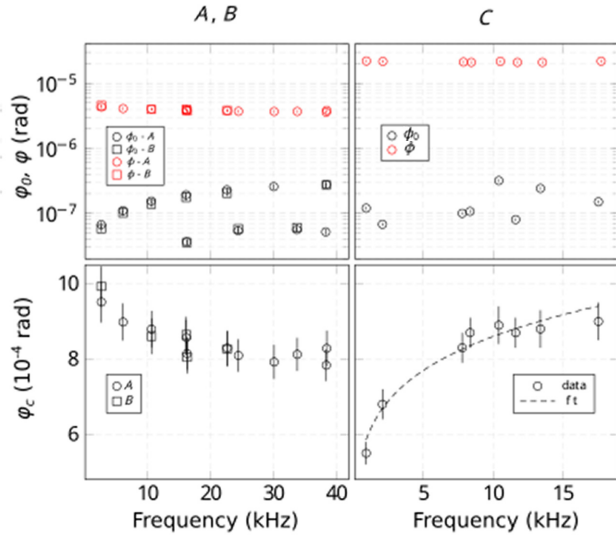
FIG. 8. Characterization of mechanical loss of disks A and B, coated with IBS a-SiC thin films (left column), and C, coated with MS a-SiC thin films (right column), as a function of frequency. Top row: measured loss angle before and after deposition of sputtered a-SiC thin films (φ_0 and φ, respectively). Bottom row: coating loss angle φ_c of as-deposited IBS (left) and MS (right) a-SiC thin films [see Eq. (2) for more details]; for the MS a-SiC coating samples, the best-fit power-law model of Eq. (5) is also shown (dashed line).

whose mass m_0 before coating could only be deduced from known sample properties, the resulting large uncertainties on its dilution factor D invalidated our fitting procedure. Therefore, we cannot provide any meaningful estimations of Y and ν for the MS a-SiC coatings.

Overall, the loss angle of the sputtered a-SiC coatings is a few times higher than that of the as-deposited high-index layers of current GWDs [15].

VI. MOLECULAR DYNAMIC SIMULATIONS

A. Model and methods

In order to model from a microscopic point of view the observed mechanical properties of our films, we develop a numerical analysis of the structure and properties of amorphous SiC. Classical molecular dynamics simulations are carried out using LAMMPS software [48]. We model SiC using an effective interatomic potential consisting of two-

and three-body interactions. The potential energy of the system is given by

$$V = \sum_{i<j} V_{ij}^{(2)}(r_{ij}) + \sum_{i,j<k} V_{jik}^{(3)}(r_{ij}, r_{ik}), \qquad (6)$$

where r_{ij} is the distance between ith and jth atoms. The two-body term $V_{ij}^{(2)}(r_{ij})$ includes steric repulsion between ions, Coulomb repulsion due to charge-transfer effects between ions, charge-dipole interactions due to electronic polarizability of ions and van der Waals interactions. The three-body term $V_{jik}^{(3)}(r_{ij}, r_{ik})$ is written as the product of a bond stretching and bending dependence. Full details about the interatomic potential, including the specific values of the parameters, are given in Ref. [49].

Each simulation consists of 10 648 atoms contained in a cubic box with periodic boundary conditions. The structure of an amorphous solid sample is obtained by simulating a steep cooling from a high-temperature liquid. The simulated silicon carbide crystal is first equilibrated at 300 K and then rapidly heated to 5000 K. The melting of the crystal, resulting in a liquid structure, is confirmed after examining the pair distribution function. The liquid at 5000 K is equilibrated for 50 ns and then cooled down to 0 K at a constant rate within the NPT ensemble (constant number of particles N, pressure P, and temperature T). Different values of the cooling rate are considered. During the quench run, configurations at the temperatures of interest are collected, equilibrated again for 50 ps and finally energy minimized. With this protocol, we generate 20 independent samples for each cooling rate.

Macroscopic elastic moduli are obtained following the quasistatic deformation protocol [50]. The system is deformed in small increments $\delta\epsilon = 10^{-5}$ followed by energy minimization at fixed applied strain via a conjugate gradient method. The deformation is performed until the applied strain reached $\epsilon = 0.005$, which is small enough to ensure that the system deforms elastically and the corresponding stress-strain curve is linear. The values of the bulk modulus K and shear modulus G are obtained from the slopes of the curves in the case of isotropic bulk deformation and shear deformation, respectively. Assuming isotropic behavior, the Young modulus E and the Poisson ratio ν can be estimated as $E = 9KG/(3K + G)$ and $\nu = (3K - 2G)/(2(3K + G))$, respectively.

TABLE III. Measured mechanical properties of a-SiC sputtered thin films: density ρ (see Sec. III A 1), best-fit Young modulus Y and Poisson ratio ν of the IBS samples and best-fit parameters (a, b) of the power-law model used to describe the data of the coating loss angle of MS samples [see Eq. (5) for more details].

	ρ (g/cm³)	Y (GPa)	ν	a (10^{-4} rad)	b
Disk A		273 ± 1	0.22 ± 0.02		
Disk B	2.87 ± 0.01	276 ± 2	0.20 ± 0.01		
Disk C	2.82 ± 0.05			8.6 ± 0.3	0.16 ± 0.03

Mechanical loss is directly obtained using dynamical mechanical spectroscopy (DMS) on the simulated system. DMS is performed by imposing to the simulation box a tensile strain $\epsilon_{ii}(t)$ in the i direction ($i = X, Y, Z$), which follows a sinusoidal dependence on time t, $\epsilon_{ii}(t) = \epsilon_0 \sin(\omega t)$, with ϵ_0 being the amplitude of the deformation and ω the pulse, and measuring the corresponding tensile stress along the same direction, σ_{ii}. No deformation of the simulation box takes place in the other directions. The results are averaged over all three directions. We fix the strain amplitude $\epsilon_0 = 0.01$, such that the deformation is in the linear elastic regime. The frequency-dependent quality factor $Q(f)$ is determined by the ratio $Q(f) = E'(f)/E''(f)$, where $E'(f)$ and $E''(f)$ are the storage and the dissipative parts of the dynamic elastic modulus. The inverse quality factor Q^{-1} is a direct estimate of the loss angle φ since $Q^{-1} \approx \varphi$ holds in the case of small mechanical loss.

B. Results

1. Competition between crystallization and glass formation

In Fig. 9 we show for a given sample the evolution of the potential energy per atom U/N (left panel) and density ρ (right panel) upon cooling for different quench rates, ranging from 10^3 to 10^5 K/ns. We observe that for the slowest cooling rate 10^3 K/ns both the energy and the density exhibit a sharp change at about 2000 K. This is the signature of crystallization occurring in the system, confirmed by direct visual inspection of the sample, i.e., the visualization of atomic configurations achieved via a specific software for simulations (OVITO), which features apparent ordered structures (not shown). Crystallization occurs also for a faster rate 5×10^3 K/ns, though changes are less marked. This behavior is common to all the 20 samples we consider. As the experimental results indicate that our samples are amorphous, we have an indication that a proper representation of our SiC films must be obtained by employing sufficiently fast cooling rates.
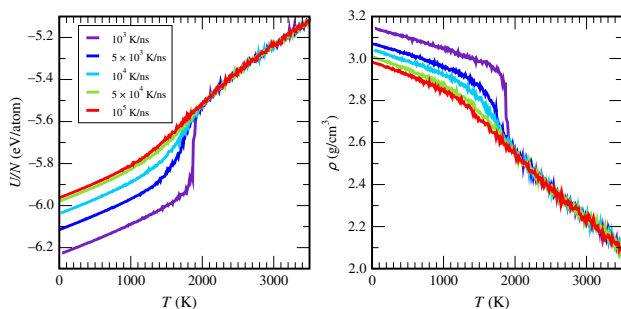

FIG. 9. Evolution of the potential energy per atom U/N (left) and density ρ (right) upon cooling for different quench rates, ranging from 10^3 to 10^5 K/ns.

Visual inspection of configurations is not sufficient to understand the evolution for rates faster than 10^5 K/ns. Therefore, we resort to statistical structural analysis based on the partial pair distribution function $g_{X-Y}(r)$ with $X, Y = $ Si,C, which is plotted in Fig. 10 for configuration at $T = 300$ K. Data are shown for different quench rates $q = 10^5$ K/ns, 5×10^4 K/ns, 10^4 K/ns and corresponds to the average over 20 independent samples for each rate. For comparison we also show the pair distribution function for a fully crystallized sample produced with a rate $q = 10^3$ K/ns. For the two fastest rates 10^5 K/ns and 5×10^4 K/ns the pair distribution functions point to an amorphous structure. Conversely, for 10^4 K/ns the incipient splitting of the peak corresponding to the second coordination shell suggests the development of order in the system, which is presumably of crystalline nature. A rough estimate of the crystalline fraction in our system can be obtained using the method proposed in Ref. [51], which allows one to identify cubic and hexagonal crystalline order. We find that for 10^4 K/ns the crystalline fraction in the 20 independent samples range from 50% to 80% whereas it is less than 10% and less than 5% in the samples produced with rates 5×10^4 K/ns and 10^5 K/ns, respectively.

Finally, we note that, due to the limited accessible timescales, simulated cooling rates are several order of magnitude faster than experimental deposition rates. While depositing a film with a thickness corresponding to the size of the simulation box would ideally require about 10^{-2} s while quenching it from the melt takes about 10^{-9} s in simulated time. Yet, despite this gap and the fundamental differences in modeling deposition as a quenching process, recently MD simulations are shown to provide a reliable estimate of the mechanical losses in films of amorphous tantala [52,53].

2. Mechanical properties

In this section we report the results on the modeling of the dynamical response of amorphous SiC samples. We focus on samples quenched with a cooling rate 5×10^4 K/ns. This choice represents a compromise between a fast quench rate, which limits the crystalline fraction in the system, as previously discussed, and a slow quench rate, which is known to result in more relaxed samples, with lower mechanical losses [52]. Further, SiC samples produced with this cooling rate have a density $\rho = 2.98$ g/cm^3, which is in reasonable agreement with the experimental value of a-SiC thin films grown via IBS and MS techniques.

First, we calculate the elastic properties of SiC samples. We obtain $E = 274 \pm 1$ GPa and $\nu = 0.21 \pm 0.01$ for the Young modulus and the Poisson ratio, respectively, in agreement with values measured on the IBS samples
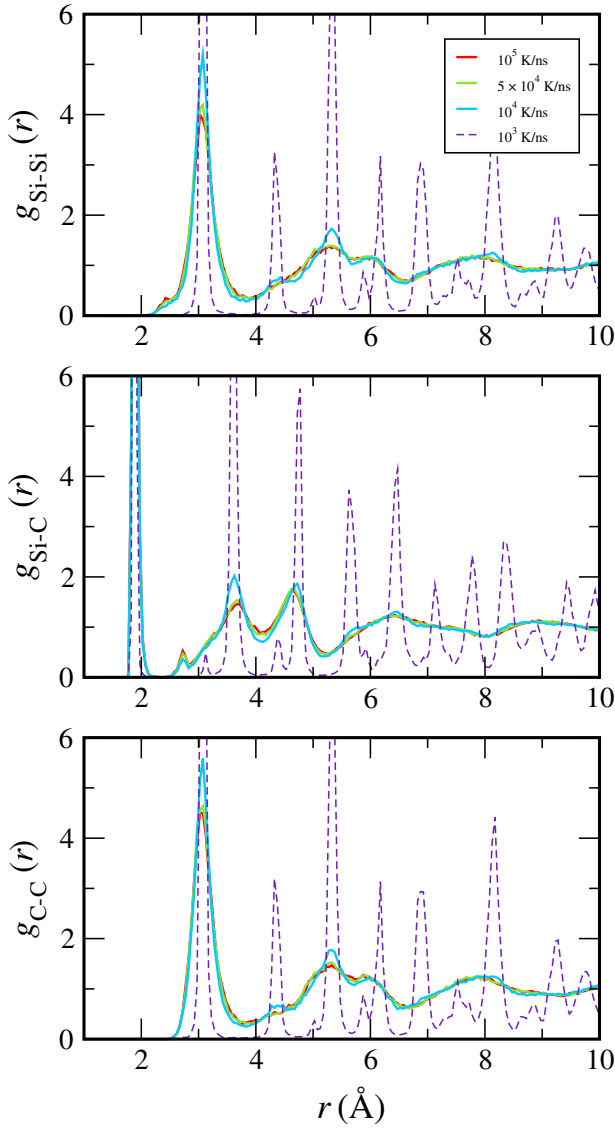
FIG. 10. Partial pair distribution function at $T = 300$ K. Data are shown for different quench rates and corresponds to the average over 20 independent samples for each rate.

FIG. 11. Frequency dependence of the coating loss angle $\varphi_c = Q^{-1}$, where Q is the quality factor obtained from molecular dynamics simulations; the dashed line is the best fit curve with a power-law equation $\varphi_c \propto f^b$ in the GHz range. *Inset*: low-frequency extrapolation of the power-law regime of φ_c; the vertical line marks the value $f = 1$ KHz.

loss angle in the acoustic region (see the inset of Fig. 11). We find $\varphi_c(f = 1 \text{ kHz}) = Q^{-1}_{1\,\text{kHz}} = 2.34 \times 10^{-3} \pm 0.3 \times 10^{-3}$, which is of the same order of magnitude of our experimental results.

VII. CONCLUSIONS

In this work we produce and study thin films of a-SiC to evaluate the viability of this material for the realization of coatings with ultralow optical and mechanical losses for their use in ultrasensitive optical apparatuses, in particular, in GWDs.

Several samples of SiC thin films are successfully grown in their amorphous form, as demonstrated by GIXRD data, using two different sputtering systems. Samples produced via MS exhibit a tendency to grow poor of Si, with a typical Si:C ratio around 0.74, while IBS samples are nearly stoichiometric. The Si deficiency in the MS system could, however, be easily cured by enriching the Si content on the target. Apart from this aspect, the two sets of samples presented a very similar density, and a morphology whose differences can be attributed to the different substrates used.

From the optical point of view, our results show that the obtained films present a certain level of variability in the optical constants, which seems however not to be related to differences in composition or on the production method, either MS or IBS. The fact that aging or annealing can contribute to lowering the values of the optical constants suggests that as-deposited samples are in a sort of nonstabilized state and that the observed variability of the optical constants can be attributed to this initial nonequilibrium condition. Anyway, all the analyzed a-SiC films display an absorption level, which is at least 5 orders of magnitude

(see Sec. V A). In Fig. 11 we show the frequency dependence of the loss angle φ_c, computed as the inverse quality factor Q^{-1} in the range accessible to molecular dynamics simulations. Unfortunately, this range is quite far from the one studied experimentally in Sec. V A. However, it can be noted that in the GHz range a well-defined power-law regime is found, i.e., $\varphi_c = Q^{-1} \propto f^b$ with $b = 0.14 \pm 0.01$. Remarkably, the power-law behavior, and in particular the value of the exponent b, are in reasonable agreement with the experimental results obtained on the MS samples presented in Sec. V A ($b = 0.18$), as well as on previous simulation results on amorphous tantala [52,53]. Assuming the validity of the power-law frequency dependence down to lower frequencies, we may estimate the value of the
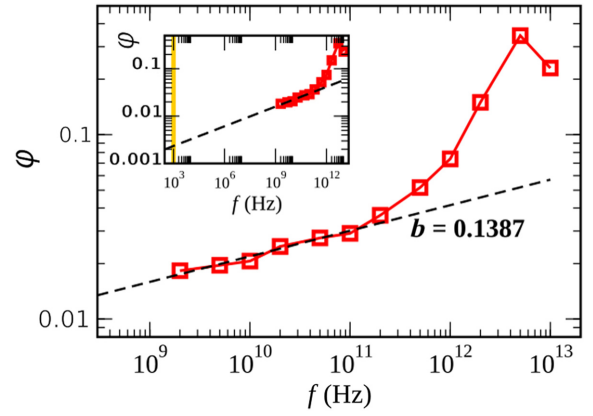
higher than the one of the current coatings used in GWDs, such as tantala-titania or silica [15,16,18]. This seems to indicate that *a*-SiC thin films are intrinsically much more absorbing in the infrared range than their crystalline bulk counterpart [54], for reasons that appear to be related to their amorphous structure rather than to the presence of dopants or other extrinsic factors.

The mechanical properties are measured in the range of frequencies from about 1 kHz to about 40 kHz. The MS sample exhibited a power-law dependency of the loss angle upon the frequency, similarly to what is reported in Ta_2O_5 and Ta_2O_5-TiO_2 and with a characteristic exponent $b \approx 0.18$, which is in line with previous investigations, but about a factor of 2 larger [15]. Quite surprisingly, IBS samples tested with the same method produced a qualitatively different result. It is not clear yet whether this discrepancy has to be attributed to a real difference in the thin film structure due to the different deposition method, or to some measurement issues. Further investigations on this aspect are ongoing; in particular, as optical measurements indicate that the as-deposited samples appear to be in an initial nonequilibrium condition, it will be interesting to check the effect of annealing procedures on mechanical losses. In any case, the overall loss angle for all the studied samples is very close to $\varphi \approx 10^{-3}$ rad^{-1} at 10 kHz, which is several times higher than the corresponding value for currently used low-loss high refractive-index coatings [15].

Finally, our experimental results are used as an input to develop a protocol to simulate the structure and the dynamics of amorphous SiC using a molecular dynamic approach. The procedure to generate the sample follows the same protocol already developed to simulate other low-mechanical loss materials [52,53] and consists in simulating a fast quenching of a SiC volume starting from a high-temperature liquid state. By selecting the proper cooling rate we succeed in obtaining a model, which is in large part amorphous and displaying a density very close to the experimentally measured one. Furthermore, the model is able to correctly reproduce the power-law dependence of the mechanical losses on the frequency, as it is experimentally observed in our MS samples, with a coherent estimation of the characteristic exponent and of the order of magnitude of the losses in the acoustic frequency region, of interest for gravitational-wave science.

The main conclusion of this work is that amorphous SiC, despite its favorable properties, seems not competitive with respect to other materials used in ultralow optical and mechanical loss experiments. However, the interest in amorphous SiC remains due to its wide range of applications. We thus believe that the data obtained along this work and, in particular, the molecular dynamics model could serve as valuable resources for further developments in this sense.

[1] N. Ledermann, J. Baborowski, P. Muralt, N. Xantopoulos, and J.-M. Tellenbach, Sputtered silicon carbide thin films as protective coating for MEMS applications, Surf. Coat. Technol. **125**, 246 (2000).

[2] A. Raza, A. S. Alketbi, R. Devarapalli, H. Li, and T. Zhang, Refractory ultrathin nanocomposite solar absorber with superior spectral selectivity and thermal stability, Adv. Opt. Mater. **8**, 2000679 (2020).

[3] J. B. Kortright and D. L. Windt, Amorphous silicon carbide coatings for extreme ultraviolet optics, Appl. Opt. **27**, 2841 (1988).

[4] M. Naftaly, J. F. Molloy, B. Magnusson, Y. M. Andreev, and G. V. Lanskii, Silicon carbide $-$ a high-transparency nonlinear material for THz applications, Opt. Express **24**, 2590 (2016).

[5] A. Ordine, C. Achete, O. Mattos, I. Margarit, S. Camargo, and T. Hirsch, Magnetron sputtered sic coatings as corrosion protection barriers for steels, Surf. Coat. Technol. **133-134**, 583 (2000).

[6] G. Pensl and W. Choyke, Electrical and optical characterization of SiC, Physica B **185**, 264 (1993).

[7] H. Ferhati, F. Djeffal, A. Bendjerad, L. Foughali, A. Benhaya, and A. Saidi, Highly-detective tunable band-selective photodetector based on rf sputtered amorphous sic thinfilm: Effect of sputtering power, J. Alloys Compd. **907**, 164464 (2022).

[8] H. C. Bauser, M. D. Foley, M. E. Phelan, W. Weigand, D. R. Needell, Z. C. Holman, and H. A. Atwater, Amorphous silicon carbide high contrast gratings as highly efficient spectrally selective visible reflectors, Opt. Express **30**, 26787 (2022).

[9] P. R. Saulson, *Fundamentals of Interferometric Gravitational Wave Detectors* (World Scientfic, Singapore, 2017), 2nd ed.

[10] T. J. F. M. M. Aspelmeyer and T. J. Kippenberg, Cavity optomechanics, Rev. Mod. Phys. **86**, 1391 (2014).

[11] D. G. Matei, T. Legero, S. Häfner, C. Grebing, R. Weyrich, W. Zhang, L. Sonderhouse, J. M. Robinson, J. Ye, F. Riehle, and U. Sterr, 1.5 μm Lasers with Sub-10 MHz Linewidth, Phys. Rev. Lett. **118**, 263202 (2017).

[12] J. Aasi, B. P. Abbott, R. Abbott, T. Abbott, M. R. Abernathy, K. Ackley, C. Adams, T. Adams, P. Addesso, and R. X. Adhikari *et al.*, Advanced LIGO, Classical Quantum Gravity **32**, 074001 (2015).

[13] F. Acernese, M. Agathos, K. Agatsuma, D. Aisa, N. Allemandou, A. Allocca, J. Amarni, P. Astone, G. Balestri, and G. Ballardin, Advanced VIRGO: A secondgeneration interferometric gravitational wave detector, Classical Quantum Gravity **32**, 024001 (2014).

[14] Y. Aso, Y. Michimura, K. Somiya, M. Ando, O. Miyakawa, T. Sekiguchi, D. Tatsumi, and Hiroaki Yamamoto, K. Collaboration, Interferometer design of the KAGRA gravitational wave detector, Phys. Rev. D **88**, 043007 (2013).

[15] M. Granata, A. Amato, L. Balzarini, M. Canepa, J. Degallaix, D. Forest, V. Dolique, L. Mereni, C. Michel, L. Pinard, B. Sassolas, J. Teillon, and G. Cagnoli, Amorphous optical coatings of present gravitational-wave interferometers, Classical Quantum Gravity **37,** 095004 (2020).

[16] J. Degallaix, C. Michel, B. Sassolas, A. Allocca, G. Cagnoli, L. Balzarini, V. Dolique, R. Flaminio, D. Forest, M. Granata, B. Lagrange, N. Straniero, J. Teillon, and L. Pinard, Large and extremely low loss: The unique challenges of gravitational wave mirrors, J. Opt. Soc. Am. A **36,** C85 (2019).

[17] Alex A. Amato, Silvana Terreni, Vincent Dolique, Danièle Forest, Gianluca Gemme, Massimo M. Granata, Lorenzo Mereni, Christophe Michel, Laurent Pinard, Benoit Sassolas, Julien Teillon, Gianpietro Cagnoli, and Maurizio Canepa, Optical properties of high-quality oxide coating materials used in gravitational-wave advanced detectors, J. Phys.: Mater. **2,** 035004 (2019).

[18] Laurent Pinard, Christophe Michel, Benoit Sassolas, Laurent Balzarini, Jerome Degallaix, Vincent Dolique, Raffaele Flaminio, Danièle Forest, Massimo Granata, Bernard Lagrange, Nicolas Straniero, Julien Teillon, and Gianpietro Cagnoli, Mirrors used in the LIGO interferometers for first detection of gravitational waves, Appl. Opt. **56,** C11 (2017).

[19] P. R. Saulson, Thermal noise in mechanical experiments, Phys. Rev. D **42,** 2437 (1990).

[20] Y. Levin, Internal thermal noise in the LIGO test masses: A direct approach, Phys. Rev. D **57,** 659 (1998).

[21] X. Liu, D. R. Queen, T. H. Metcalf, J. E. Karel, and F. Hellman, Hydrogen-Free Amorphous Silicon with no Tunneling States, Phys. Rev. Lett. **113,** 025503 (2014).

[22] H. B. Callen and R. F. Greene, On a theorem of irreversible thermodynamics, Phys. Rev. **86,** 702 (1952).

[23] M. Granata, A. Amato, G. Cagnoli, M. Coulon, J. Degallaix, D. Forest, L. Mereni, C. Michel, L. Pinard, B. Sassolas, and J. Teillon, Progress in the measurement and reduction of thermal noise in optical coatings for gravitational-wave detectors, Appl. Opt. **59,** A229 (2020).

[24] A. Amato, S. Terreni, M. Granata, C. Michel, B. Sassolas, L. Pinard, M. Canepa, and G. Cagnoli, observation of a correlation between internal friction and Urbach energy in amorphous oxides thin films, Sci. Rep. **10,** 1 (2020).

[25] G. M. Harry, M. R. Abernathy, A. E. Becerra-Toledo, H. Armandula, E. Black, K. Dooley, M. Eichenfield, C. Nwabugwu, A. Villar, and D. R. M. Crooks *et al.*, Titania-doped tantala/silica coatings for gravitational-wave detection, Classical Quantum Gravity **24,** 405 (2006).

[26] Www.lnl.infn.it.

[27] Www.io.csic.es.

[28] G. Vignaud and A. Gibaud, Reflex: A program for the analysis of specular x-ray and neutron reflectivity data, J. Appl. Crystallogr. **52,** 201 (2019).

[29] V. Heera, F. Prokert, N. Schell, H. Seifarth, W. Fukarek, M. Voelskow, and W. Skorupa, Density and structural changes in SiC after amorphization and annealing, Appl. Phys. Lett. **70,** 3531 (1997).

[30] A.-L. Barabási and H. E. Stanley *et al.*, *Fractal Concepts in Surface Growth* (Cambridge university press, Cambridge, 1995).

[31] L. R. Doolittle, Algorithms for the rapid simulation of Rutherford backscattering spectra, Nucl. Instrum. Methods Phys. Res., Sect. B **9,** 344 (1985).

[32] M. Prato, A. Chincarini, G. Gemme, and M. Canepa, Gravitational waves detector mirrors: Spectroscopic ellipsometry study of Ta_2O_5 films on SiO_2 substrates, Thin Solid Films **519,** 2877 (2011).

[33] G. Jellison and f.A. Mondine, Parameterization of the optical functions of amorphous materials in the interband region, Appl. Phys. Lett. **69,** 371 (1996).

[34] S. Zollner, J. G. Chen, E. Duda, T. Wetteroth, S. R. Wilson, and J. N. Hilfiker, Dielectric functions of bulk 4H and 6H SiC and spectroscopic ellipsometry studies of thin sic films on Si, J. Appl. Phys. **85,** 8353 (1999).

[35] M. Le Contellec, J. Richard, A. Guivarc'h, E. Ligeon, and J. Fontenille, Effects of the silicon-to-carbon ratio and the hydrogen content in amorphous SiC thin films prepared by reactive sputtering, Thin Solid Films **58,** 407 (1979).

[36] J. I. Larruquert, A. P. Pérez-Marín, S. García-Cortés, L. R. de Marcos, J. A. Aznárez, and J. A. Méndez, Self-consistent optical constants of SiC thin films, J. Opt. Soc. Am. A **28,** 2340 (2011).

[37] J. F. E. Pascual, J. L. Andújar, and E. Bertran, Optical and structural characterization of hydrogenated amorphous silicon carbide thin films prepared by r.f. plasma chemical vapour deposition, Diamond Relat. Mater. **4,** 1205 (1995).

[38] P. Musumeci, R. Reitano, L. Calcagno, F. Roccaforte, A. Makhtari, and M. G. Grimaldi, Relaxation and crystallization of amorphous silicon carbide probed by optical measurements, Philos. Mag. B **76,** 323 (1997).

[39] A. S. Nowick and B. S. Berry, *Anelastic Relaxation in Crystalline Solids* (Academic Press, New York and London, 1972).

[40] Tianjun Li, Felipe A. Aguilar Sandoval, Mickael Geitner, Ludovic Bellon, Gianpietro Cagnoli, Jérôme Degallaix, Vincent Dolique, Raffaele Flaminio, Danièle Forest, Massimo Granata, Christophe Michel, Nazario Morgado, and Laurent Pinard, Measurements of mechanical thermal noise and energy dissipation in optical dielectric coatings, Phys. Rev. D **89,** 092004 (2014).

[41] E. Cesarini, M. Lorenzini, E. Campagna, F. Martelli, F. Piergiovanni, F. Vetrano, G. Losurdo, and G. Cagnoli, A "gentle" nodal suspension for measurements of the acoustic attenuation in materials, Rev. Sci. Instrum. **80,** 053904 (2009).

[42] G. Vajente, A. Ananyeva, G. Billingsley, E. Gustafson, A. Heptonstall, E. Sanchez, and C. Torrie, A high throughput instrument to measure mechanical losses in thin film coatings, Rev. Sci. Instrum. **88,** 073901 (2017).

[43] M. Granata, A. Amato, M. Bischi, M. Bazzan, G. Cagnoli, M. Canepa, M. Chicoine, A. Di Michele, G. Favaro, D. Forest, and others, Optical and Mechanical Properties of Ion-Beam-Sputtered MgF_2 thin Films for Gravitational-Wave Interferometers, Phys. Rev. Appl. **17,** 034058 (2022).

[44] M. Granata, E. Saracco, N. Morgado, A. Cajgfinger, G. Cagnoli, J. Degallaix, V. Dolique, D. Forest, J. Franc, C. Michel, L. Pinard, and R. Flaminio, Mechanical loss in state-of-the-art amorphous optical coatings, Phys. Rev. D **93,** 012007 (2016).

[45] K. S. Gilroy and W. A. Phillips, An asymmetric double-well potential model for structural relaxation processes in amorphous materials, Philos. Mag. B **43**, 735 (1981).

[46] F. Travasso, P. Amico, L. Bosi, F. Cottone, A. Dari, L. Gammaitoni, H. Vocca, and F. Marchesoni, Low-frequency internal friction in silica glass, Europhys. Lett. **80**, 50008 (2007).

[47] Gianpietro Cagnoli, Matteo Lorenzini, Elisabetta Cesarini, Francesco Piergiovanni, Massimo Granata, Daniel Heinert, Filippo Martelli, Ronny Nawrodt, Alex Amato, Quentin Cassar, Johannes Dickmann, Stefanie Kroker, Diana Lumaca, Christophe Malhaire, and Carol B. Rojas Hurtado, Mode-dependent mechanical losses in disc resonators, Phys. Lett. A **382**, 2165 (2018).

[48] S. Plimpton, Fast parallel algorithms for short-range molecular dynamics, J. Comput. Phys. **117**, 1 (1995).

[49] P. Vashishta, R. K. Kalia, A. Nakano, and J. P. Rino, Interaction potential for silicon carbide: A molecular dynamics study of elastic constants and vibrational density of states for crystalline and amorphous silicon carbide, J. Appl. Phys. **101**, 103515 (2007).

[50] M. Tsamados, A. Tanguy, C. Goldenberg, and J. Barrat, Local elasticity map and plasticity in a model Lennard-Jones glass, Phys. Rev. E **80**, 026112 (2009).

[51] E. Maras, O. Trushin, A. Stukowski, T. Ala-Nissila, and H. Jónsson, Global transition path search for dislocation formation in Ge on Si(001), Comput. Phys. Commun. **205**, 13 (2016).

[52] F. Puosi, F. Fidecaro, S. Capaccioli, D. Pisignano, and D. Leporini, In silico broadband mechanical spectroscopy of amorphous tantala, Phys. Rev. Res. **1**, 033121 (2019).

[53] F. Puosi, F. Fidecaro, S. Capaccioli, D. Pisignano, and D. Leporini, Non-local cooperative atomic motions that govern dissipation in amorphous tantala unveiled by dynamical mechanical spectroscopy, Acta Mater. **201**, 1 (2020).

[54] A. M. Hofmeister, K. Pitman, A. Goncharov, and A. K. Speck, Optical constants of silicon carbide for astrophysical applications. II. Extending optical functions from infrared to ultraviolet using single-crystal absorption spectra, Astrophys. J. **696**, 1502 (2009).